Supplement of The Cryosphere, 18, 4355–4378, 2024
https://doi.org/10.5194/tc-18-4355-2024-supplement

The Cryosphere Open Access EGU

Supplement of

How well can satellite altimetry and firn models resolve Antarctic firn thickness variations?

Maria T. Kappelsberger et al.

Correspondence to: Maria T. Kappelsberger (maria.kappelsberger@tu-dresden.de)

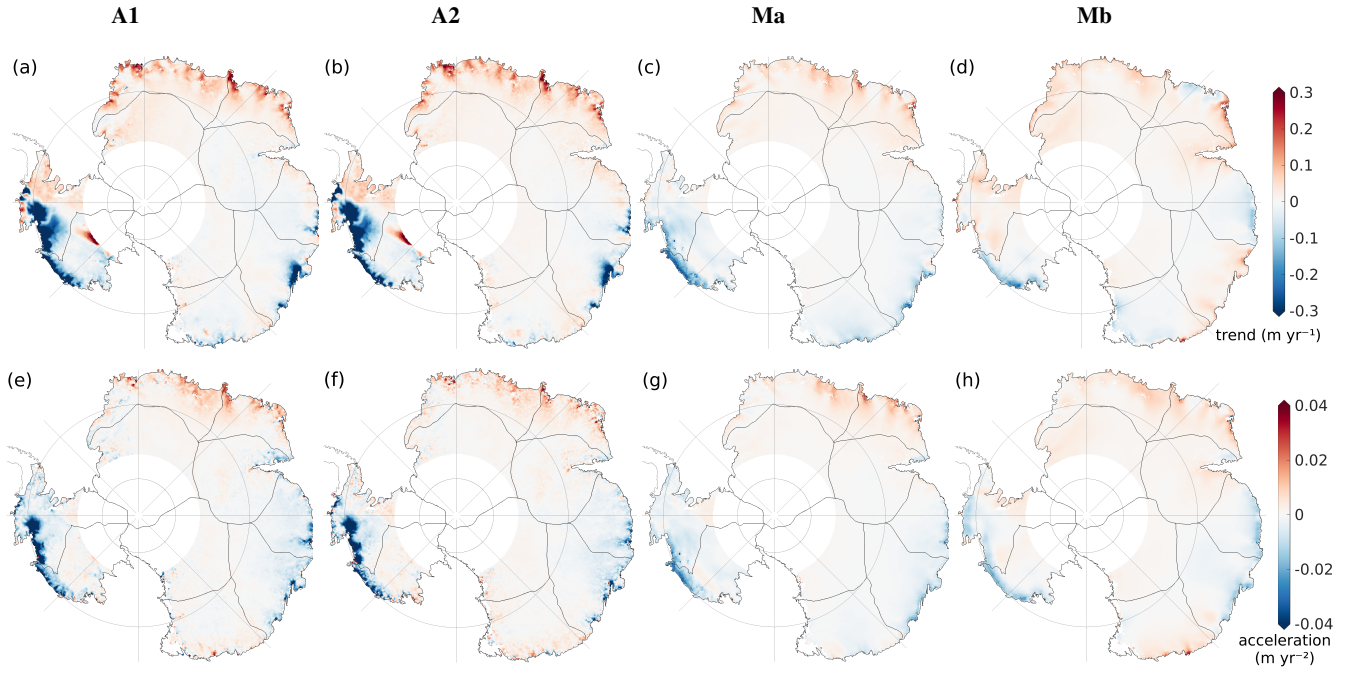

Figure S1. Subtracted parameters. (a–d) Linear and (e–h) quadratic terms adjusted to monthly elevation changes from (a, e) the altimetry product from Schröder et al. (2019) (A1, 1st column), (b, f) the altimetry product from Nilsson et al. (2022) (A2, 2nd column), (c, g) the firn model from Veldhuijsen et al. (2023) (Ma, 3rd column) and (d, h) the firn model from Medley et al. (2022) (Mb, 4th column).

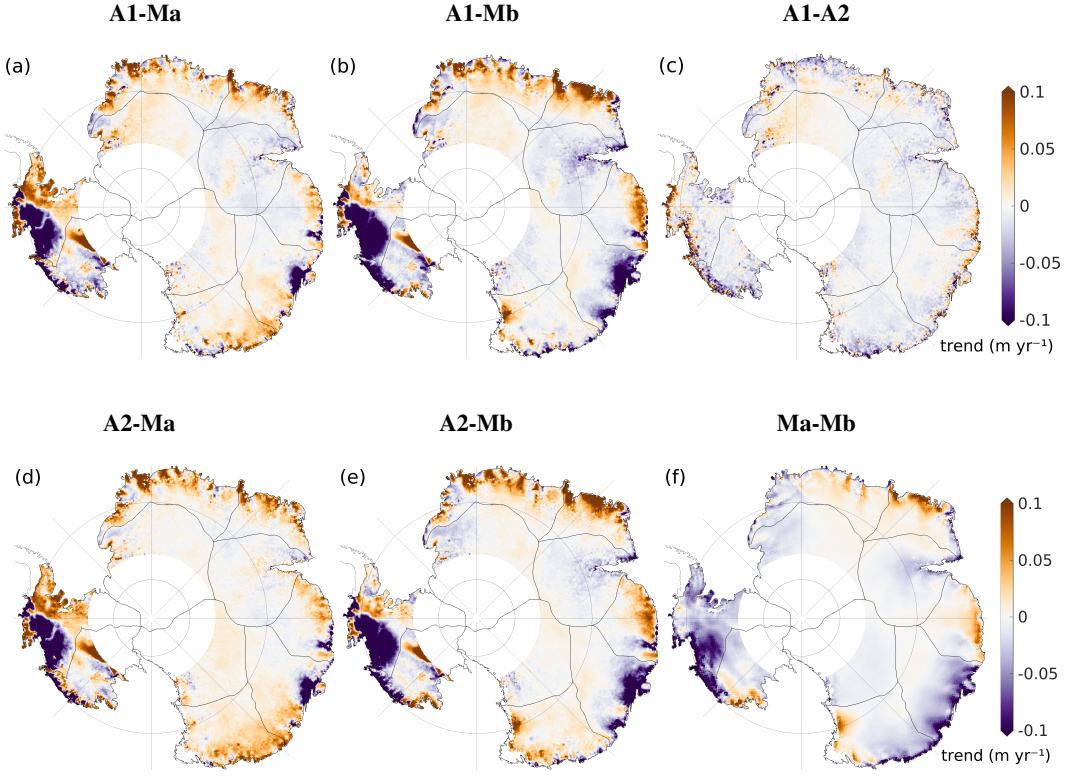

Figure S2. Differences in the linear terms.

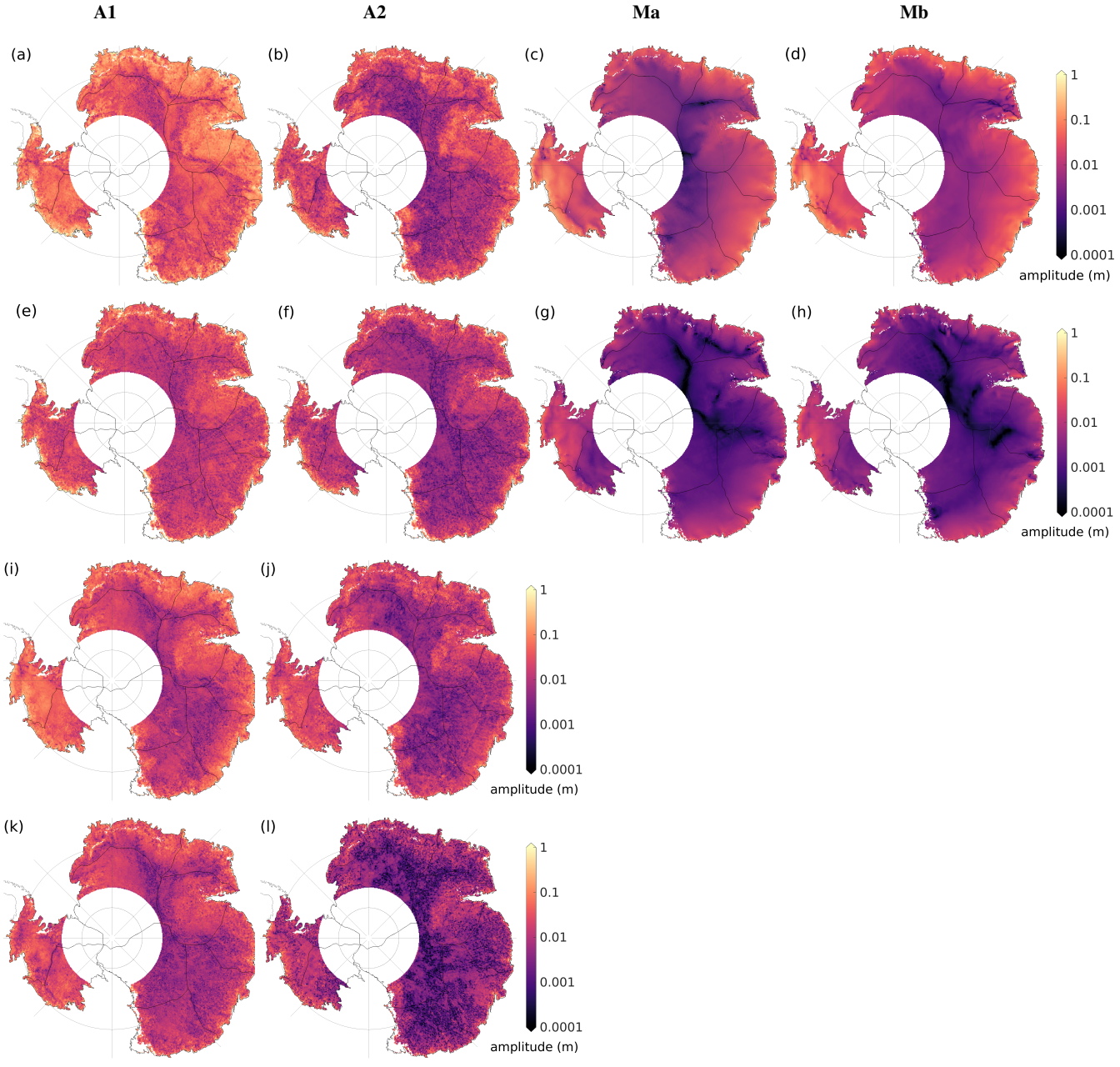

Figure S3. Subtracted parameters. (a, b) Annual amplitude before 2003, (e, f) semi-annual amplitude before 2003, (i, j) annual amplitude after 2003 and (k, l) semi-annual amplitude after 2003 adjusted to monthly elevation changes from A1 (1st column) and A2 (2nd column). (c, d) Annual amplitude of the whole period, (g, h) semi-annual amplitude of the whole period adjusted to monthly elevation changes from Ma (3rd column) and Mb (4th column).

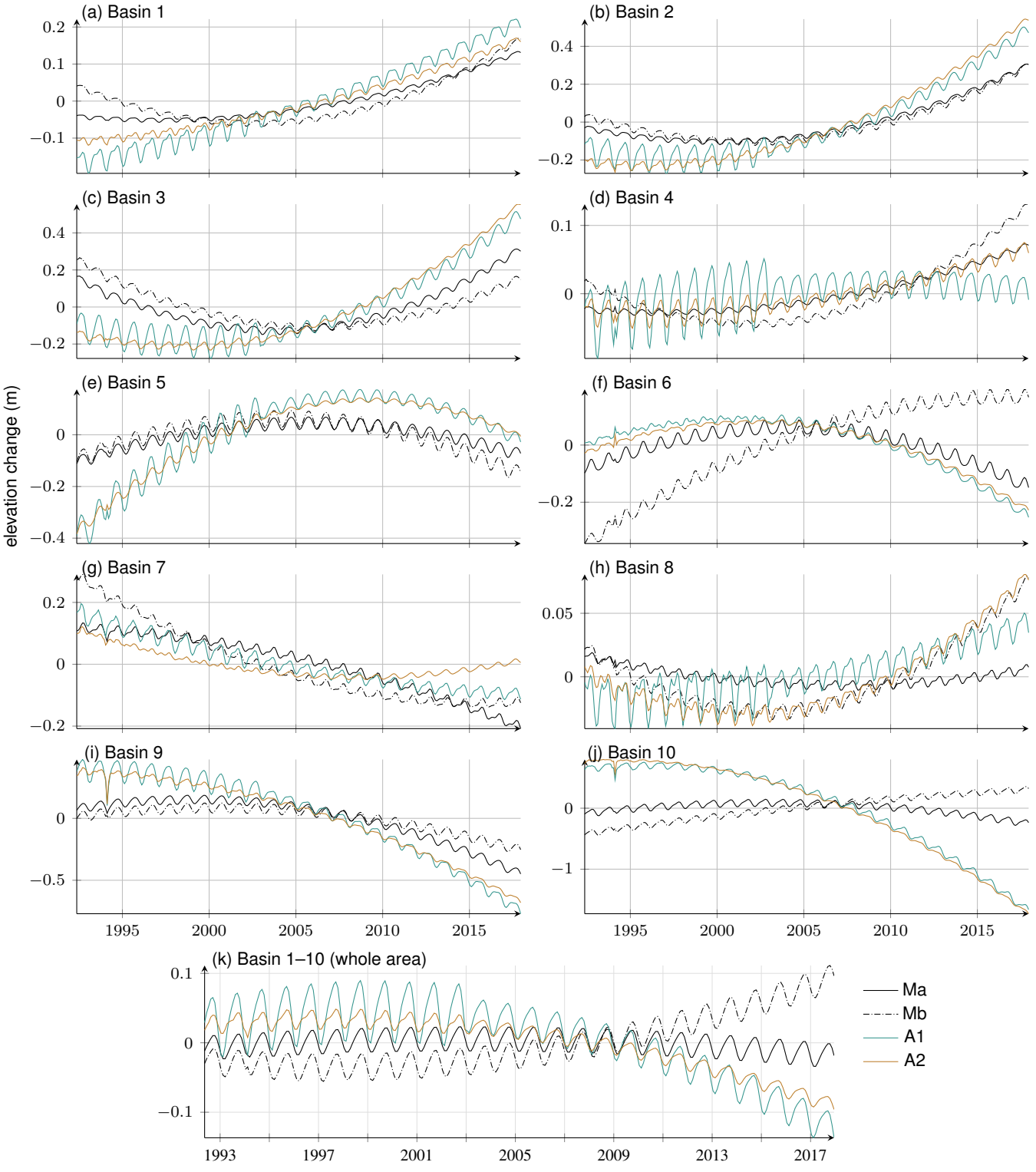

Figure S4. Basin mean time series of the adjusted linear, quadratic and seasonal model based on Ma, Mb, A1, A2. Basin definitions are shown in Fig. 3.

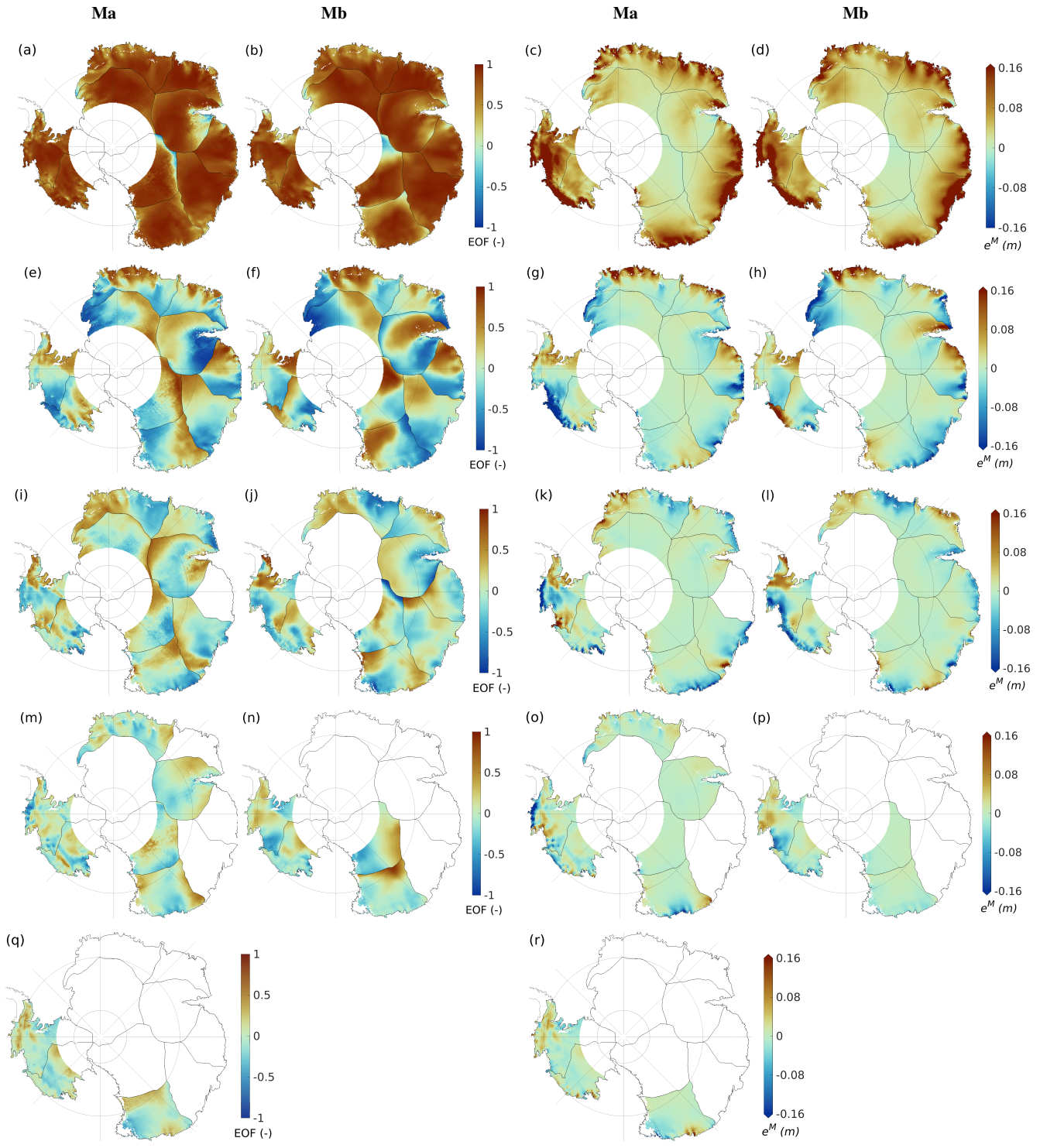

Figure S5. Dominant spatial patterns (EOFs) in firn thickness variations identified by the Ma firn model (1st column) and the Mb firn model (2nd column). EOFs are derived from standardised modelling data. 'Modelled' scaling factors $e^{\mathrm{M}}_{1\ldots5}$ from Ma (3rd column) and Mb (4th column). The 1st and 2nd columns are the same as the 3rd and 4th columns, respectively, but with restored signal amplitudes for each grid cell. (a–d) First, (e–h) second, (i–l) third, (m–p) fourth and (q, r) fifth EOFs or rather scaling factors. The corresponding temporal patterns (PCs) are given by Figs. S6 and S7 for Ma and Figs. S8 and S9 for Mb, respectively.

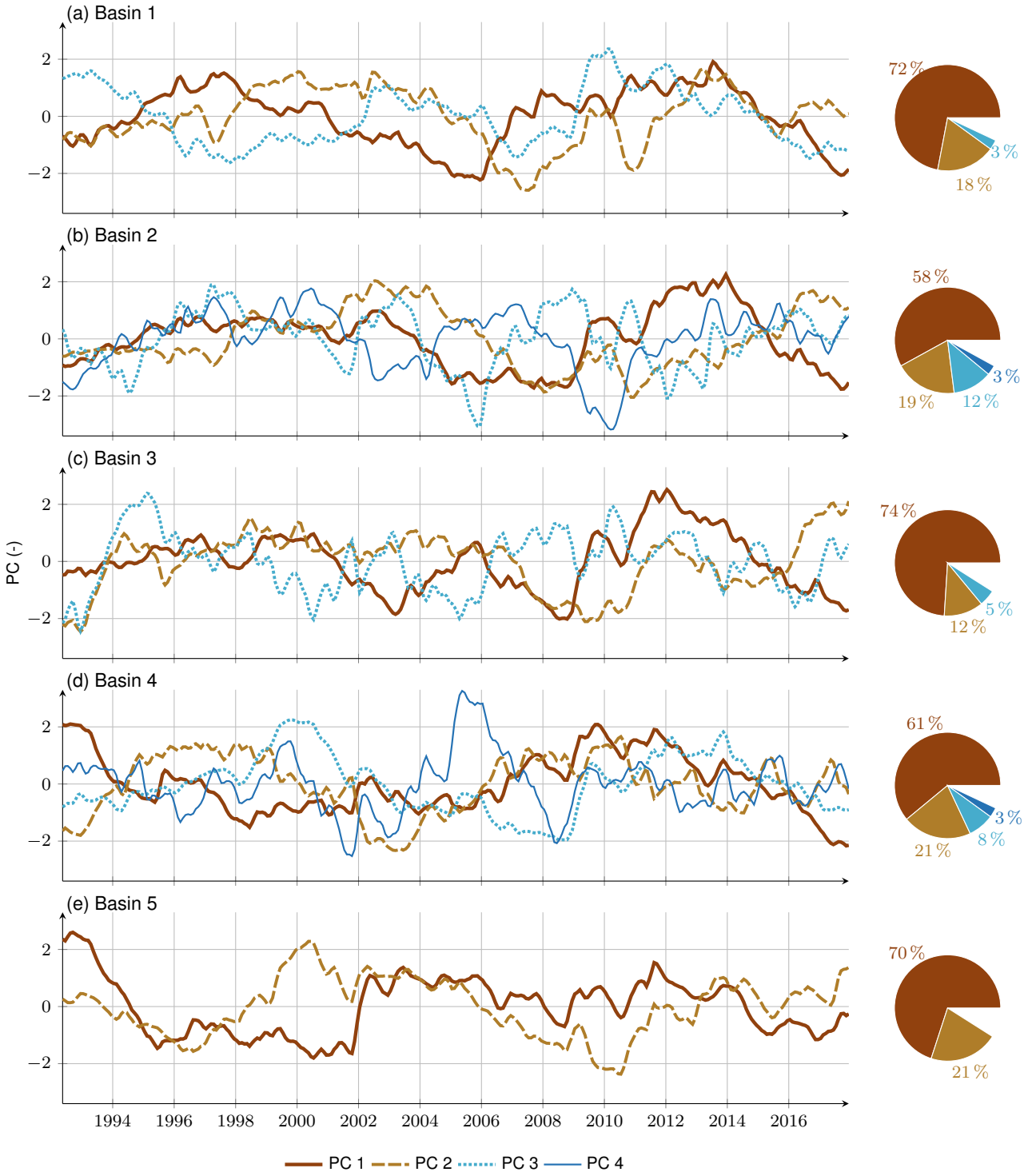

Figure S6. Dominant PCs in firn thickness variations identified by Ma for (a–d) basins 1–5 (line chart) and associated percentages of the basin's total data variance considering the respective PC/EOF pair (pie chart). The respective EOFs are given by Fig. S5 (1st column).

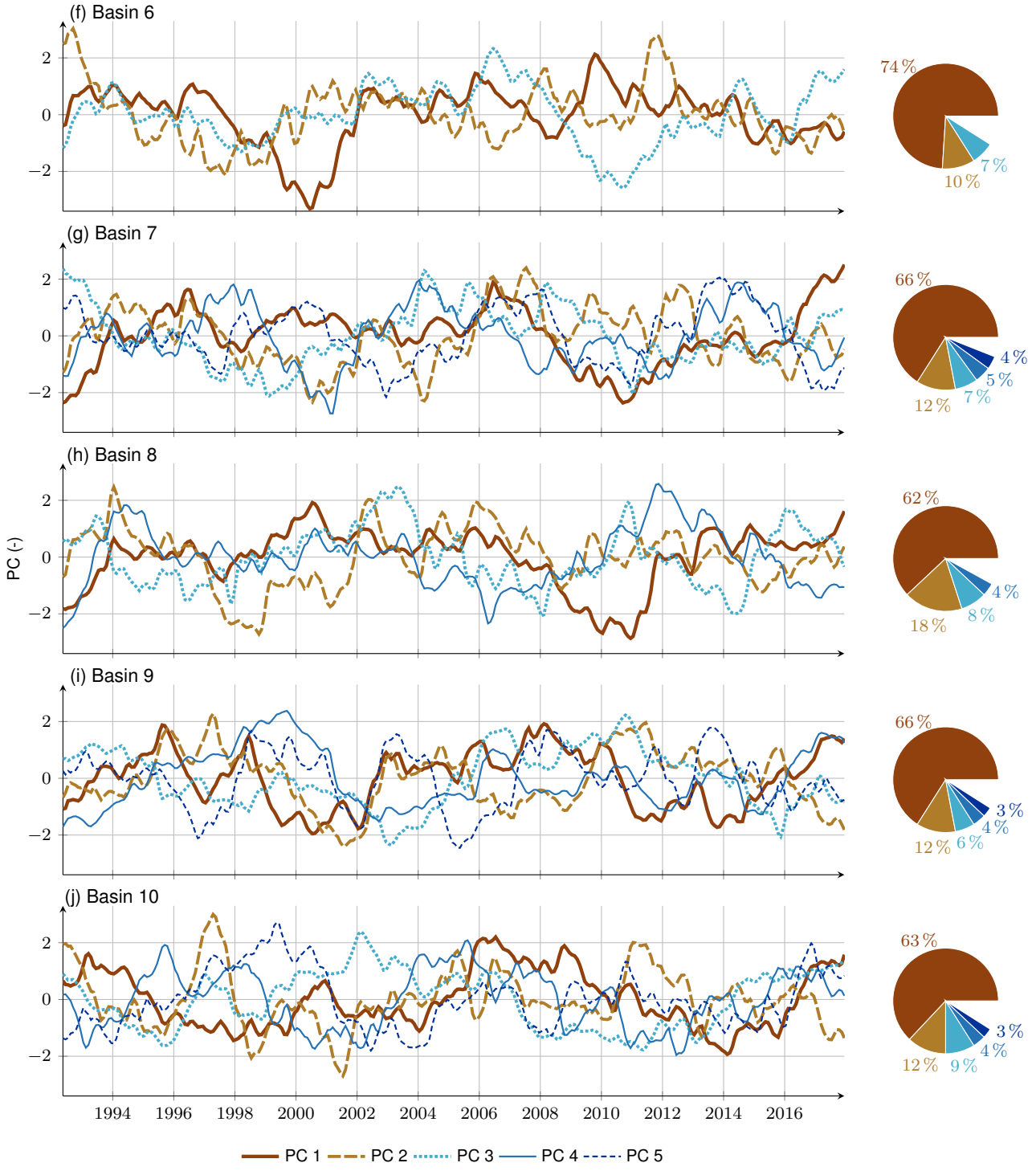

Figure S7. Dominant PCs in firn thickness variations identified by Ma for (a–d) basins 6–10 (line chart) and associated percentages of the basin's total data variance considering the respective PC/EOF pair (pie chart). The respective EOFs are given by Fig. S5 (1st column).

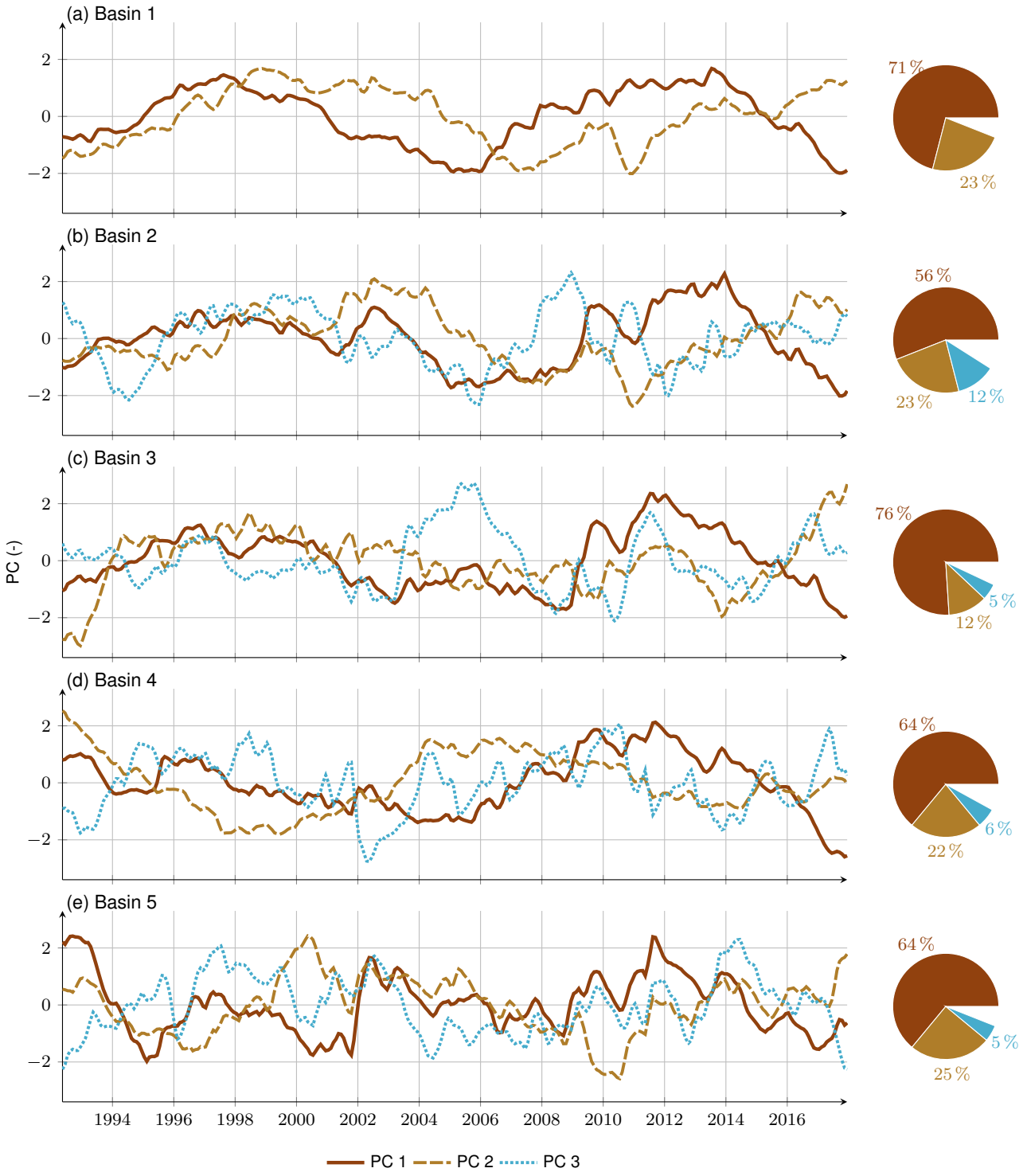

Figure S8. Dominant PCs in firn thickness variations identified by Mb for (a–d) basins 1–5 (line chart) and associated percentages of the basin's total data variance considering the respective PC/EOF pair (pie chart). The respective EOFs are given by Fig. S5 (2nd column).

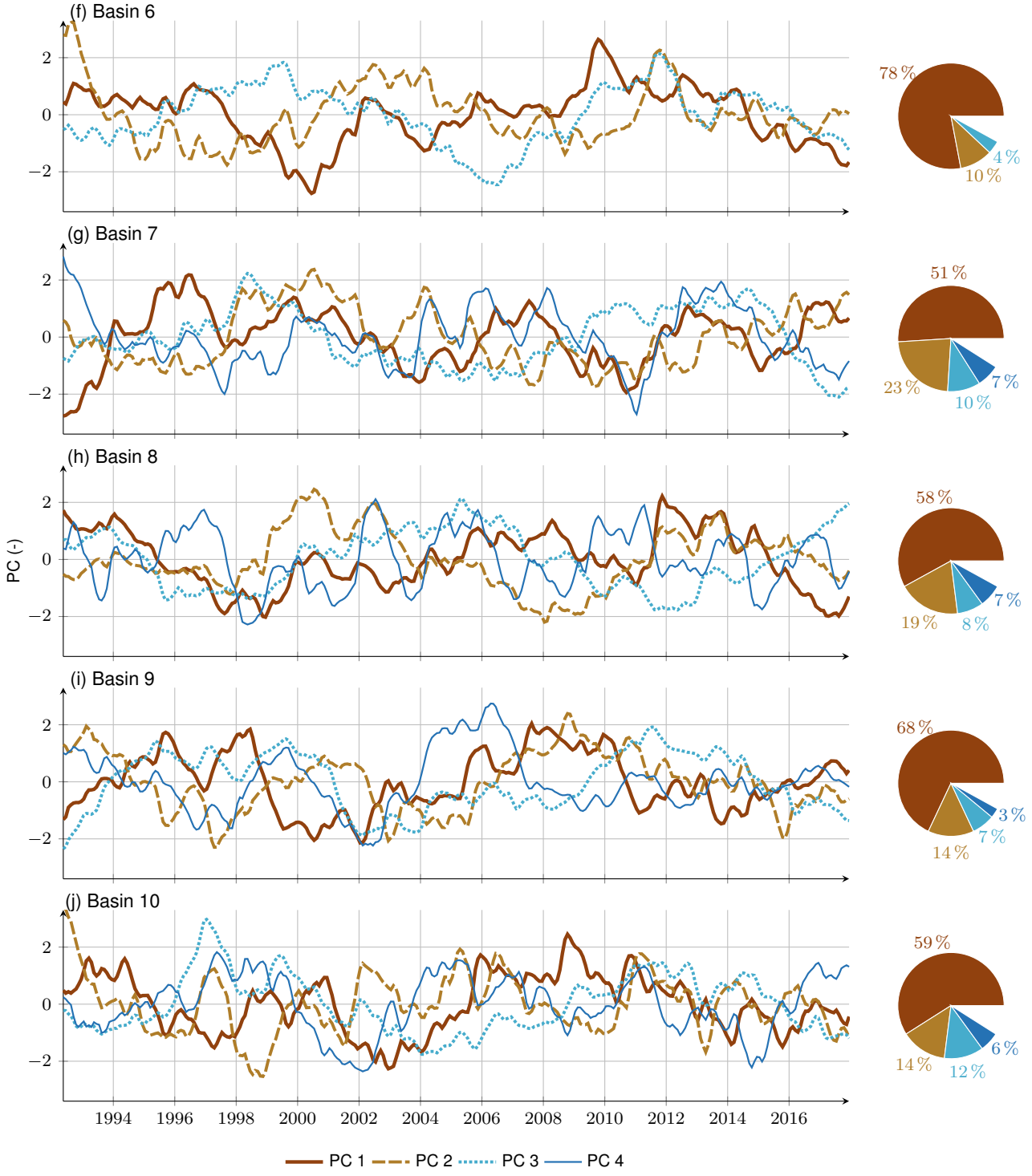

Figure S9. Dominant PCs in firn thickness variations identified by Mb for (a–d) basins 6–10 (line chart) and associated percentages of the basin's total data variance considering the respective PC/EOF pair (pie chart). The respective EOFs are given by Fig. S5 (2nd column).

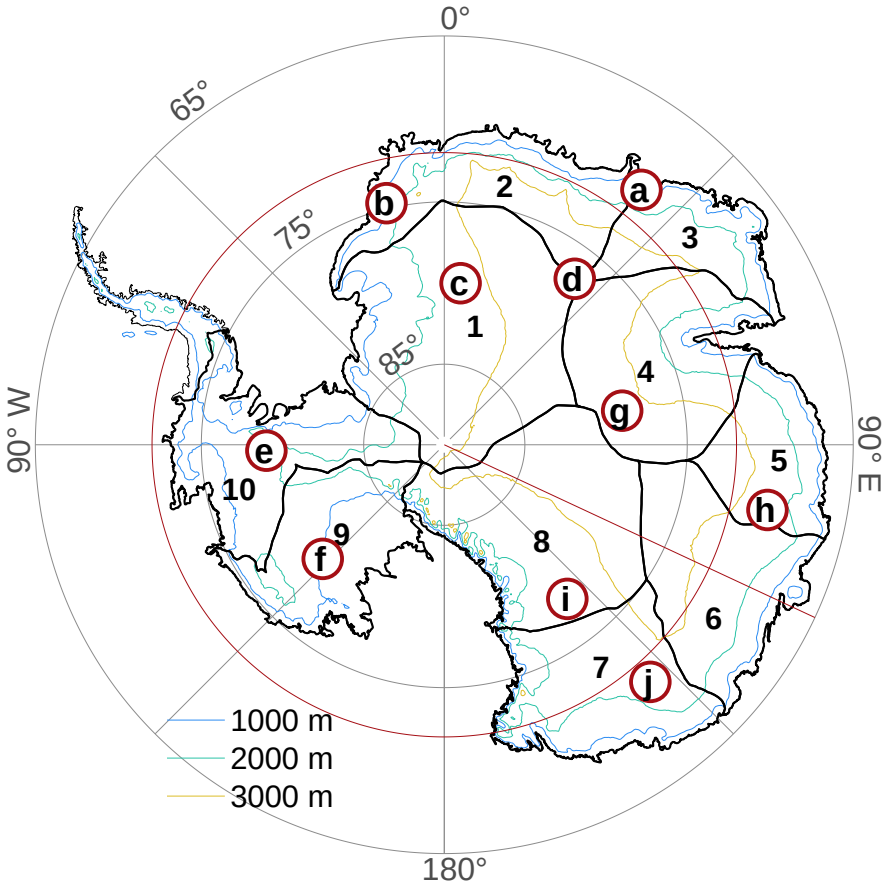

Figure S10. Subset of selected grid points a–j. Their locations were taken from Veldhuijsen et al. (2023) Fig. 9. Additionally the drainage basins of the East and West AIS used in this study (thick black lines), slightly modified from the definition of Rignot et al. (2011a, b), and the contour lines of the ice sheet surface are shown. Highlighted in red are the circle at constant latitude of 72° S (profile 1) and the line at constant longitude at 115° E (profile 2).

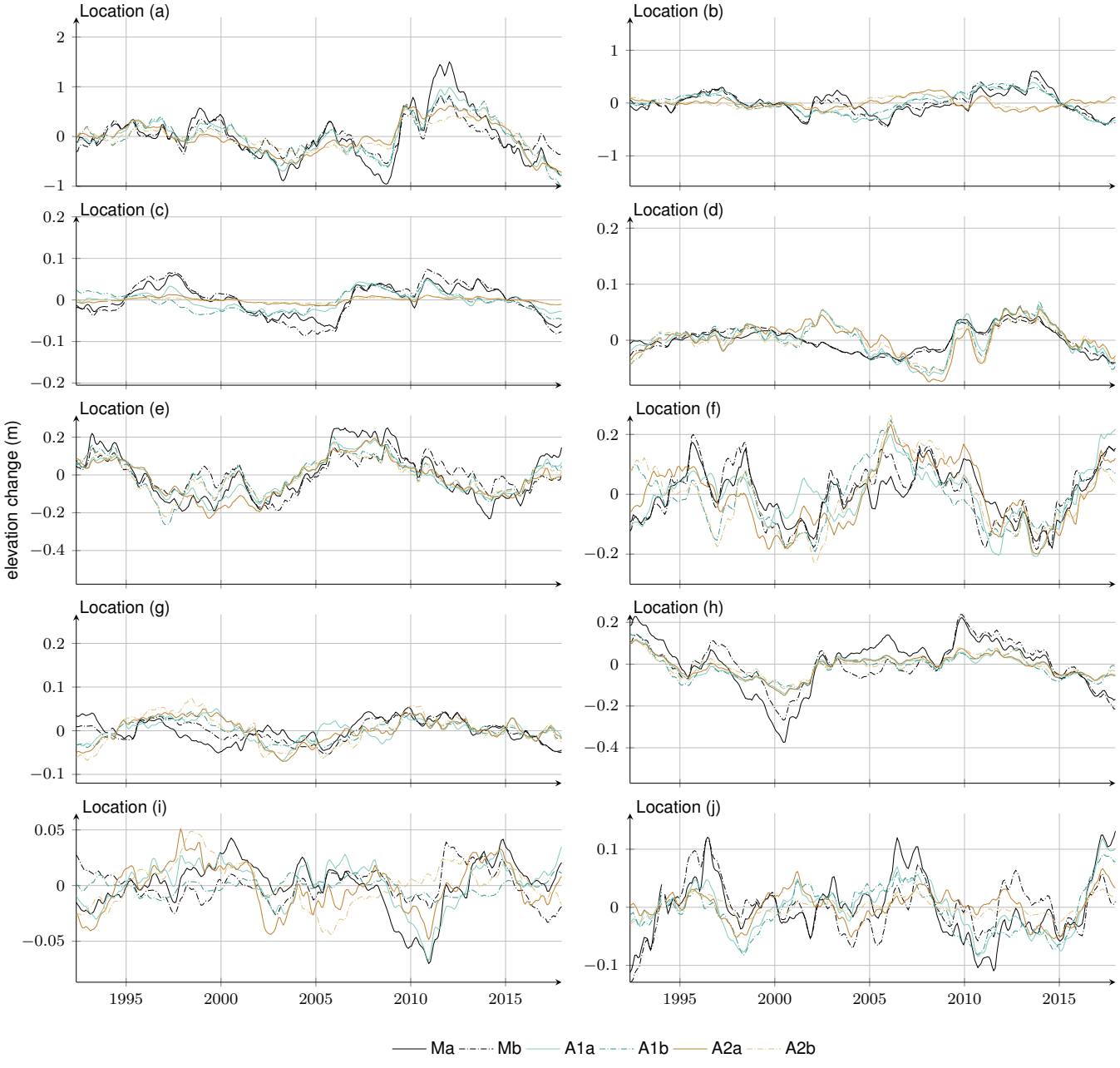

Figure S11. Time series of the modelled and adjusted firn thickness variations (fv^{Ma}, fv^{Mb} and fv^{A1a}, fv^{A2a}, fv^{A1b}, fv^{A2b}) for the subset of selected grid points a–j (Fig. S10).

Figure S12. Time series of the altimetric residuals (r^{A1a}, r^{A2a}, r^{A1b}, r^{A2b}) for the subset of selected grid points a–j (Fig. S10).

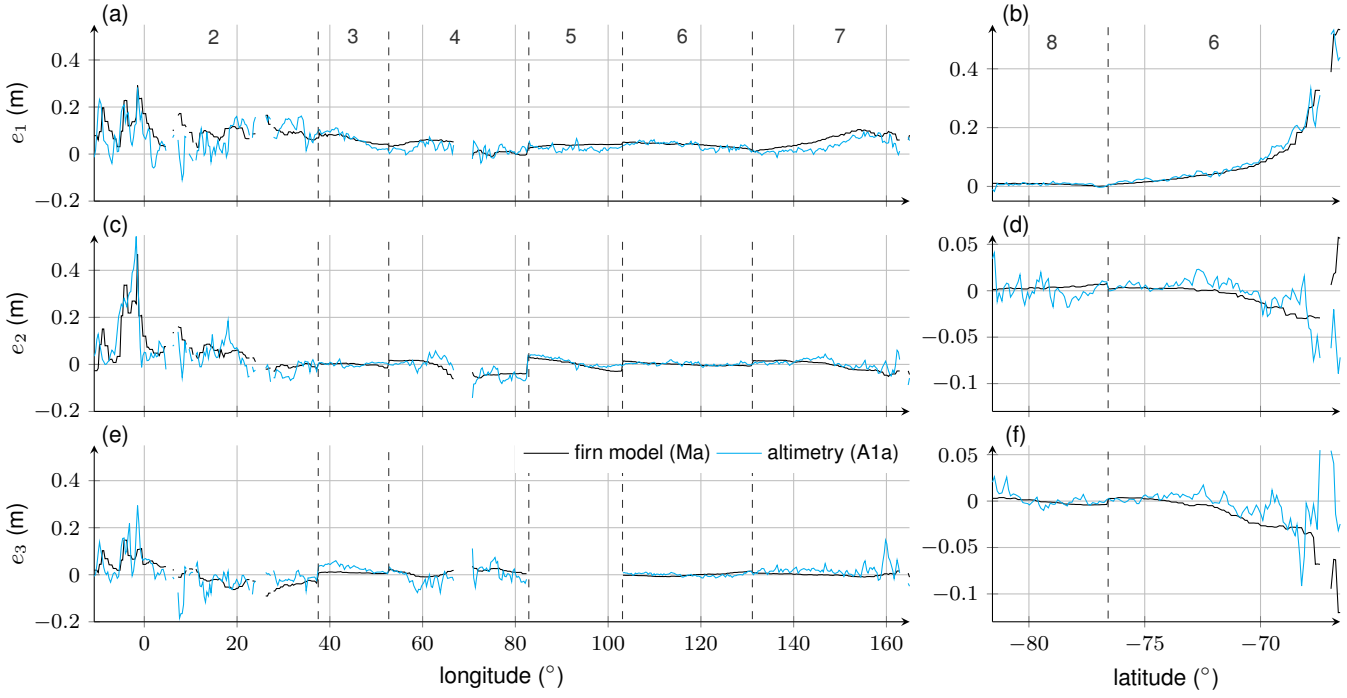

Figure S13. Scaling factors along two selected profiles (Fig. 10): profile 1 (left) and profile 2 (right). (a, b) e_1, (c, d) e_2 and (e, f) e_3. Cyan and black curves show the observed scaling factors (A1a) and the modelled scaling factors (Ma), respectively. Note the different scaling of the y-axes of profile 2.

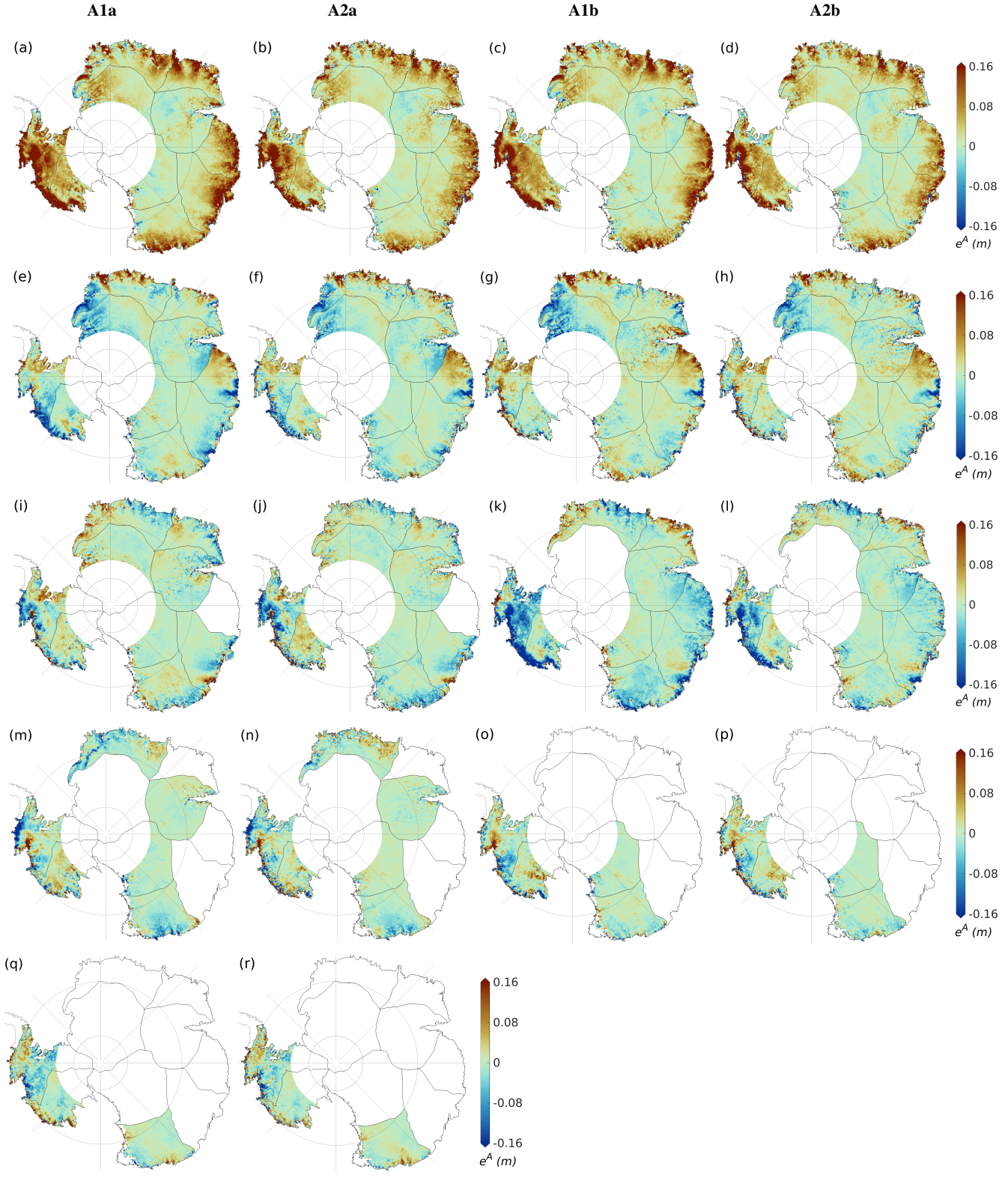

Figure S14. Observed scaling factors $e^{\mathrm{A}}_{1\ldots5}$ adjusted to monthly elevation changes from altimetry. Scaling factors given for (a–d) $\mathrm{PC}^{\mathrm{M}}_1$, (e–h) $\mathrm{PC}^{\mathrm{M}}_2$, (i–l) $\mathrm{PC}^{\mathrm{M}}_3$, (m–p) $\mathrm{PC}^{\mathrm{M}}_4$ and (q–r) $\mathrm{PC}^{\mathrm{M}}_5$ based on the four different versions: A1a (1st column), A2a (2nd column), A1b (3th column) and A2b (4th column). $e^{\mathrm{A}}_{1\ldots5}$ can be directly compared to $e^{\mathrm{M}}_{1\ldots5}$ (Fig. S5 columns 3 and 4).

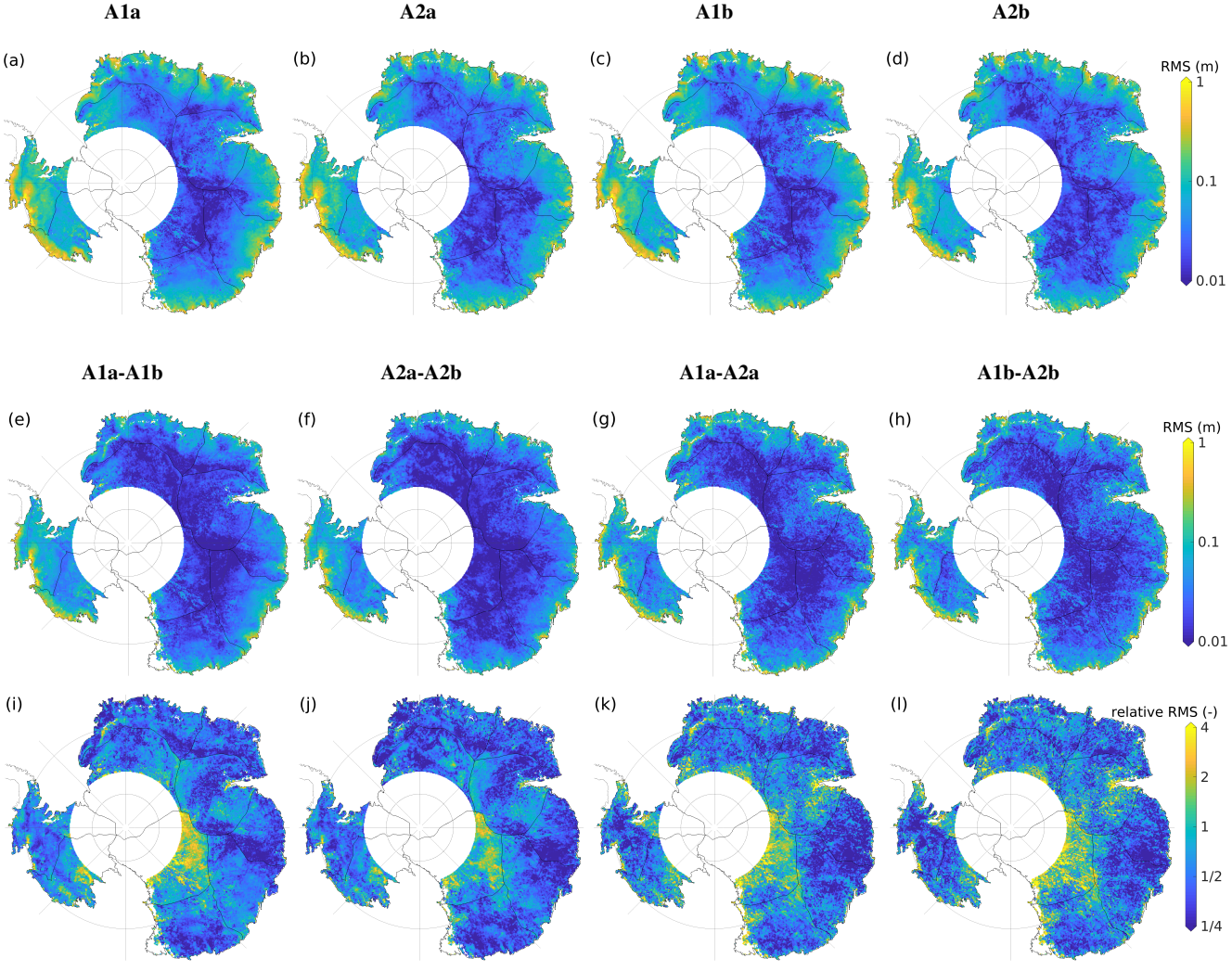

Figure S15. (a–d) Rms of the time series of adjusted firn thickness variations for the four different versions: (a) fv^{A1a}, (b) fv^{A2a}, (c) fv^{A1b} and (d) fv^{A2b}. (e–l) Rms of the time series of their differences shown (e–h) absolutely and (i–l) relatively by normalising with the rms of fv^{Ma}.

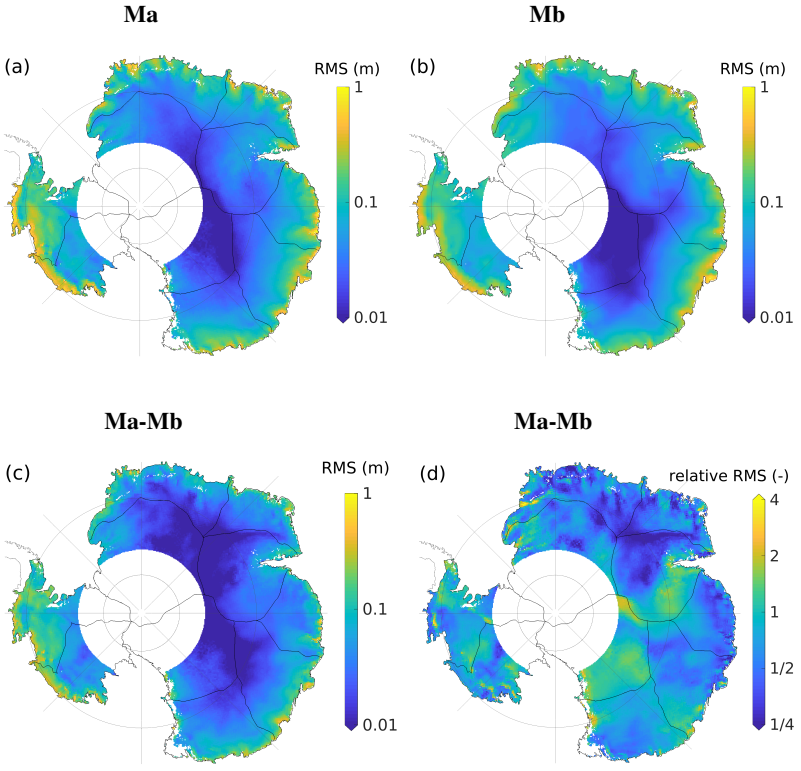

Figure S16. (a–b) Rms of the time series of modelled firn thickness variations for the two different models: (a) fv^{Ma} and (b) fv^{Mb}. (c–d) Rms of the time series of their difference shown (c) absolutely and (d) relatively by normalising with the rms of fv^{Ma}.

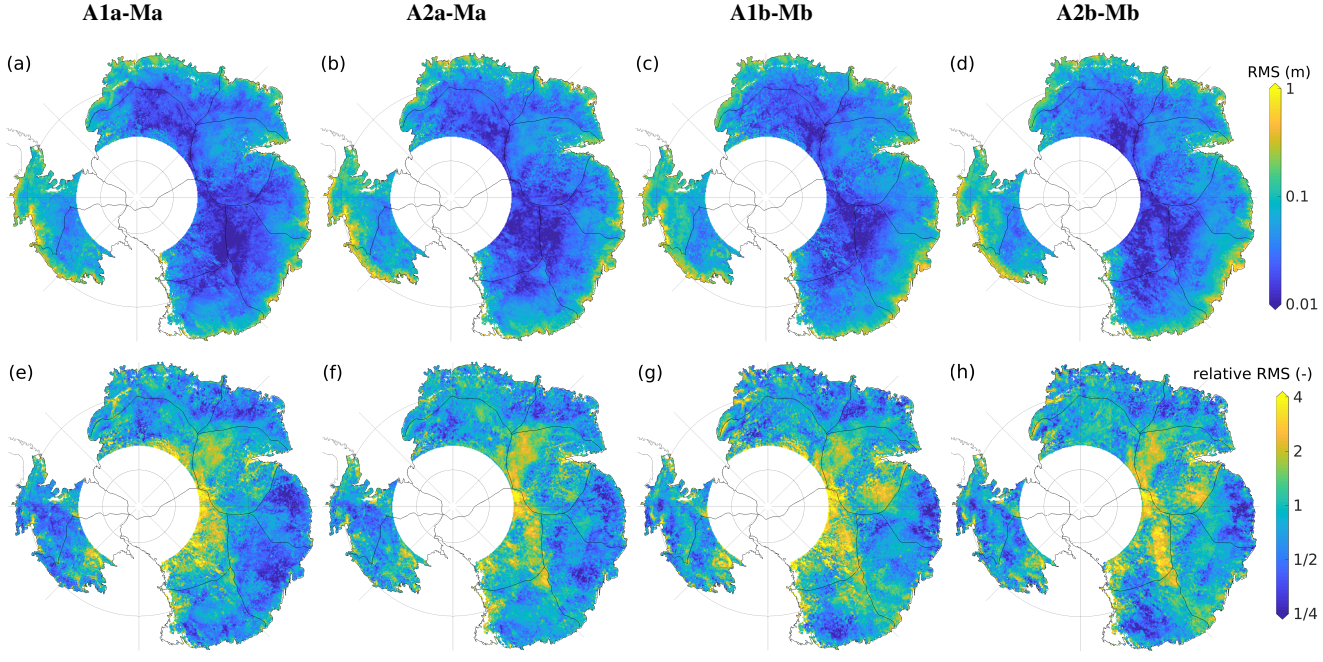

Figure S17. Rms of the time series of differences between adjusted and modelled firn thickness variations ($fv^{A} - fv^{M}$) shown (a–d) absolutely and (e–h) relatively by normalising with the rms of fv^{Ma}.

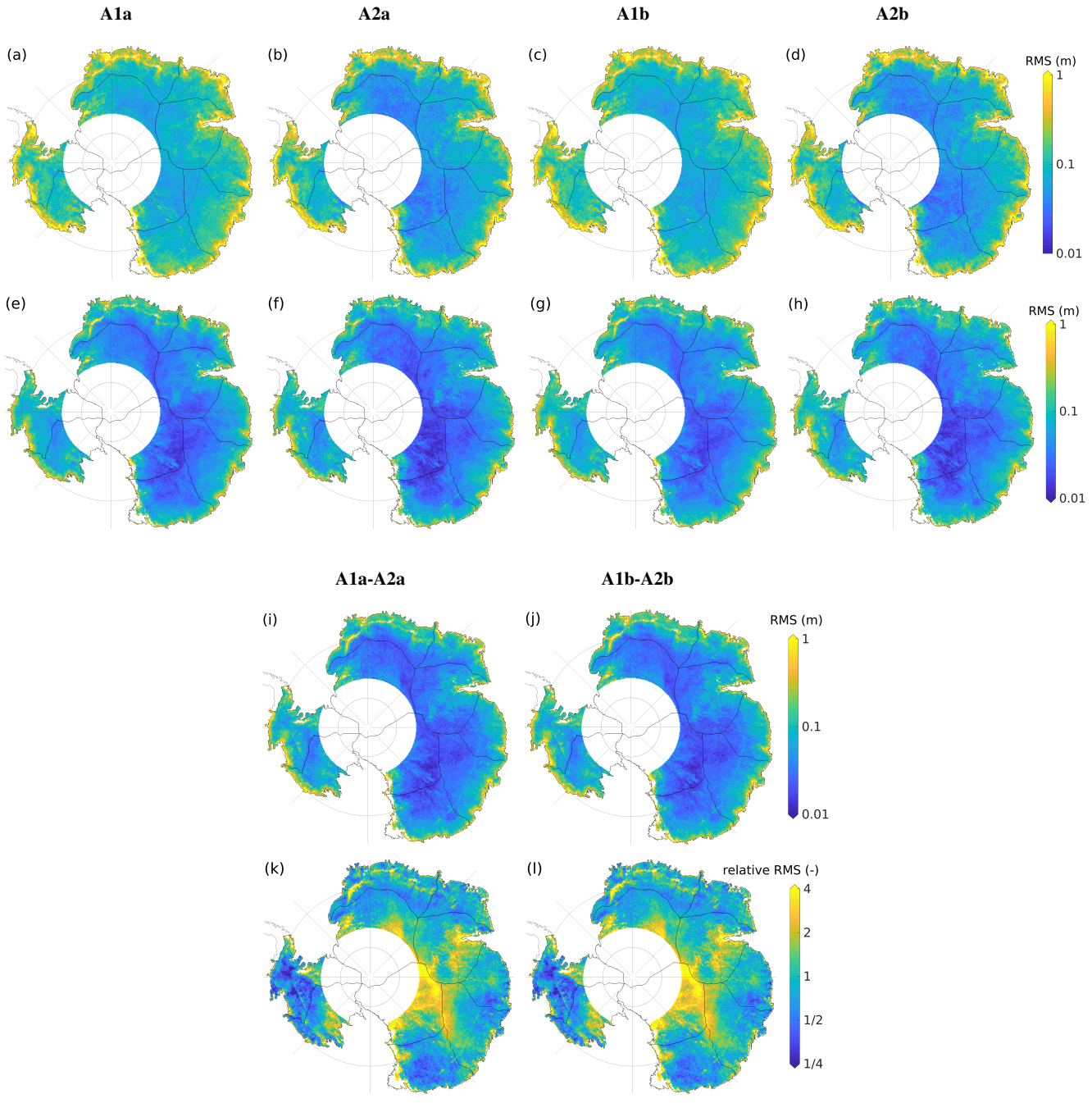

Figure S18. (a–h) Rms of the residual altimetric time series for the four different versions over the period (a–d) before 2003 and (e–h) after 2003. (e–h) Rms of the time series of their differences ($r^{A1} - r^{A2}$) w.r.t. the period after 2003 shown (e–f) absolutely and (g–h) relatively by normalising with the rms of fv^{Ma}.

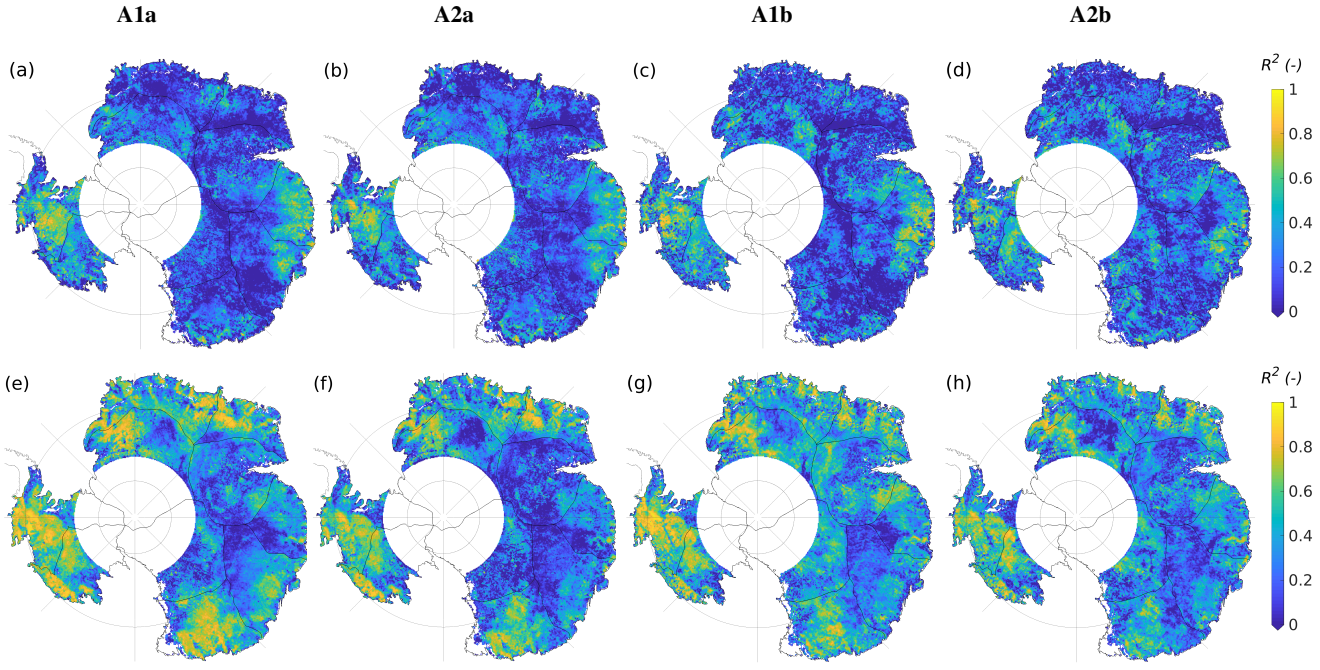

Figure S19. R-squared values, R^2, for the four different versions of regression over the period (a–d) before 2003 and (e–h) after 2003.

Table S1. Explained variance or R squared, R^2, for each basin and each version of regression (Table 1) over the period before 2003. Apart from the last column $\overline{\text{A1a}}$, R^2 is first calculated for each grid cell according to Eq. (3) and after averaged over each basin. Values of $\overline{\text{A1a}}$ are calculated by first averaging the regression results over each basin and after applying Eq. (3).

Basin	A1a	A2a	A1b	A2b	$\overline{\text{A1a}}$
1	0.22	0.22	0.24	0.26	0.41
2	0.13	0.14	0.11	0.12	0.39
3	0.10	0.07	0.11	0.09	0.47
4	0.17	0.16	0.18	0.02	0.39
5	0.41	0.39	0.35	0.26	0.82
6	0.15	0.13	0.18	0.19	0.46
7	0.17	0.13	0.20	0.18	0.44
8	0.13	0.09	0.16	0.21	0.02
9	0.30	0.33	0.25	0.32	0.47
10	0.43	0.38	0.37	0.30	0.83
1–10*	0.21	0.19	0.21	0.21	0.43

* Refers to the entire area (considered a single basin).

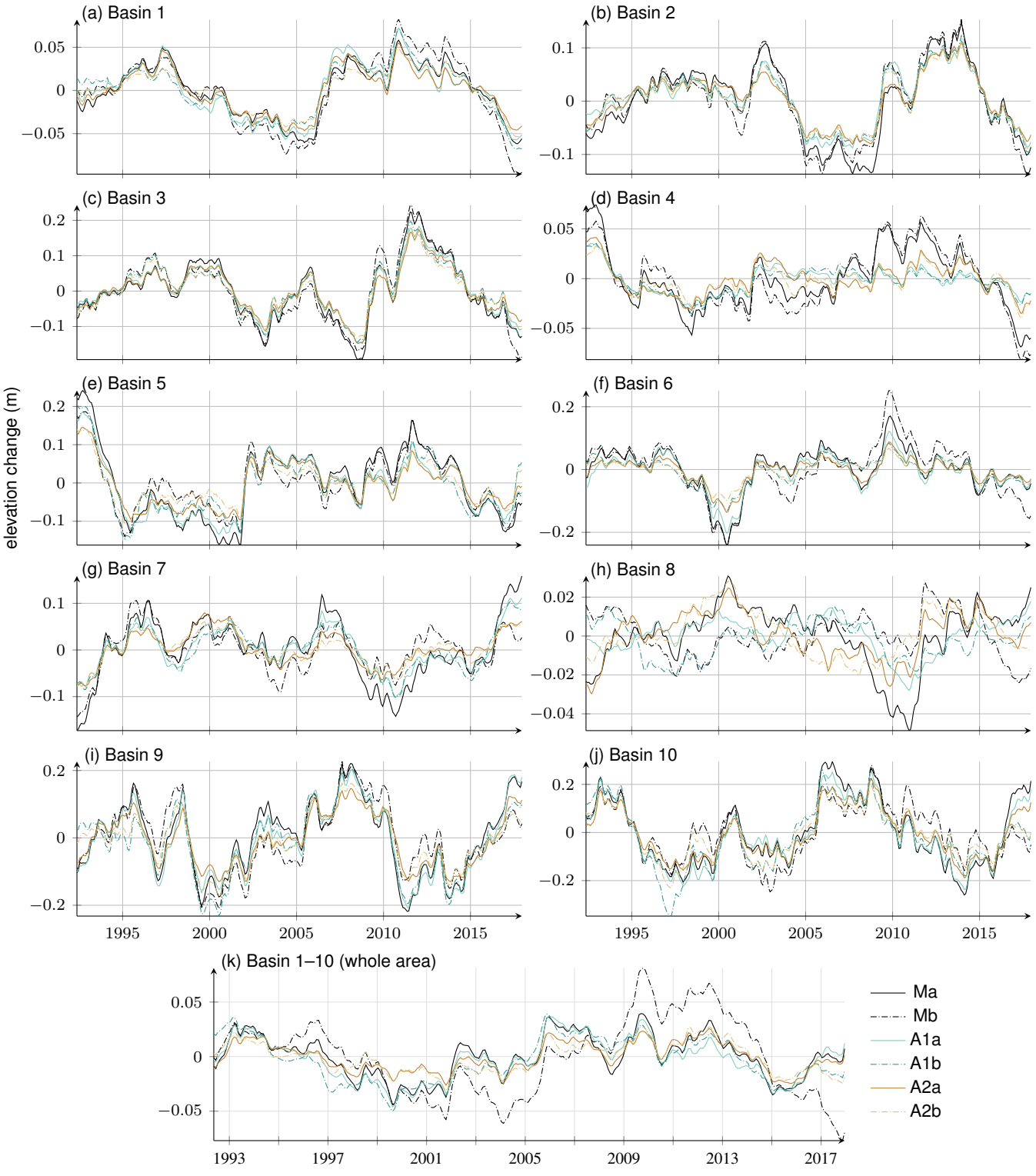

Figure S20. Basin mean time series of the modelled and adjusted firn thickness variations (fv^{Ma}, fv^{Mb} and fv^{A1a}, fv^{A2a}, fv^{A1b}, fv^{A2b}).

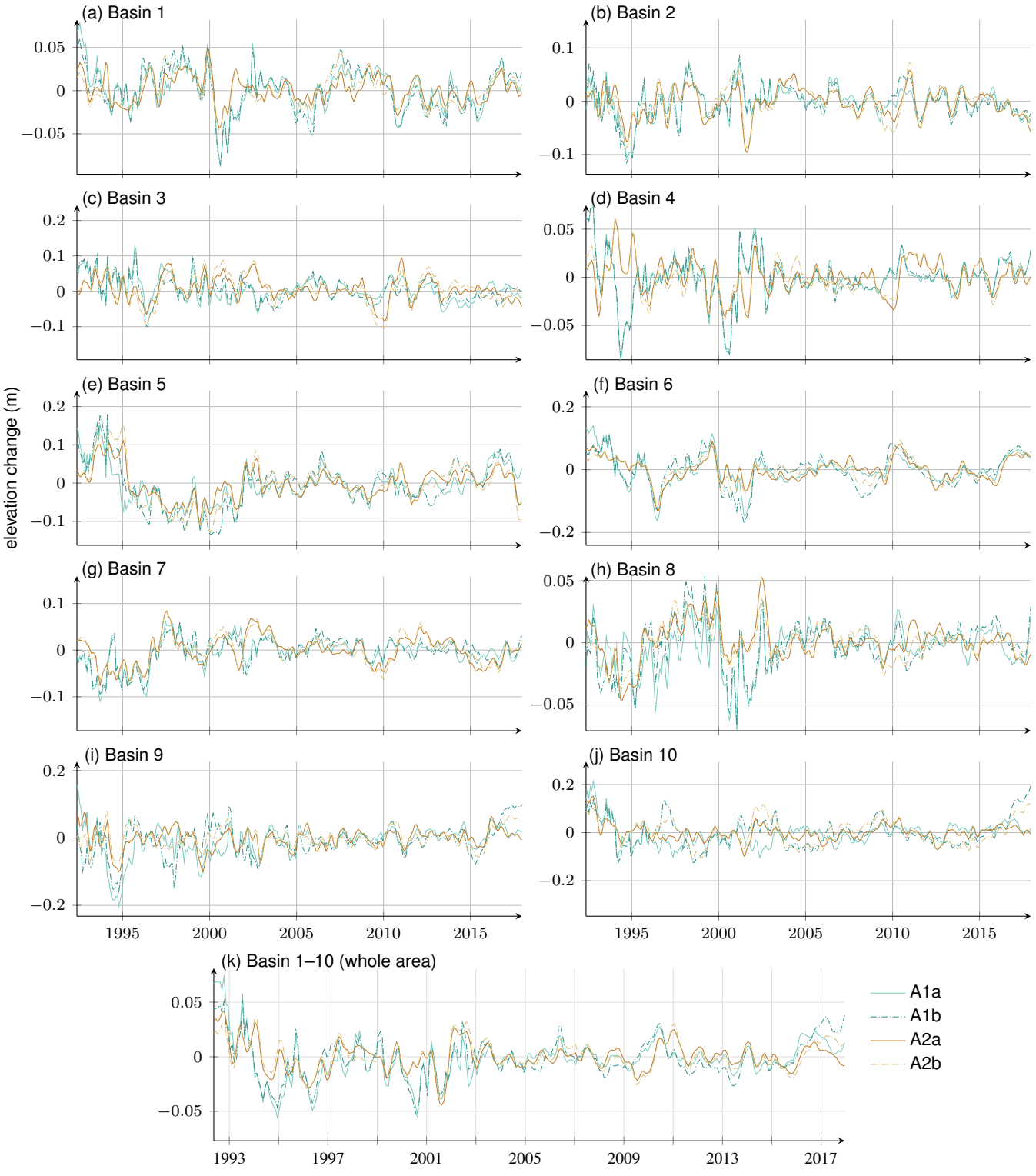

Figure S21. Basin mean time series of the altimetric residuals (r^{A1a}, r^{A2a}, r^{A1b}, r^{A2b}).

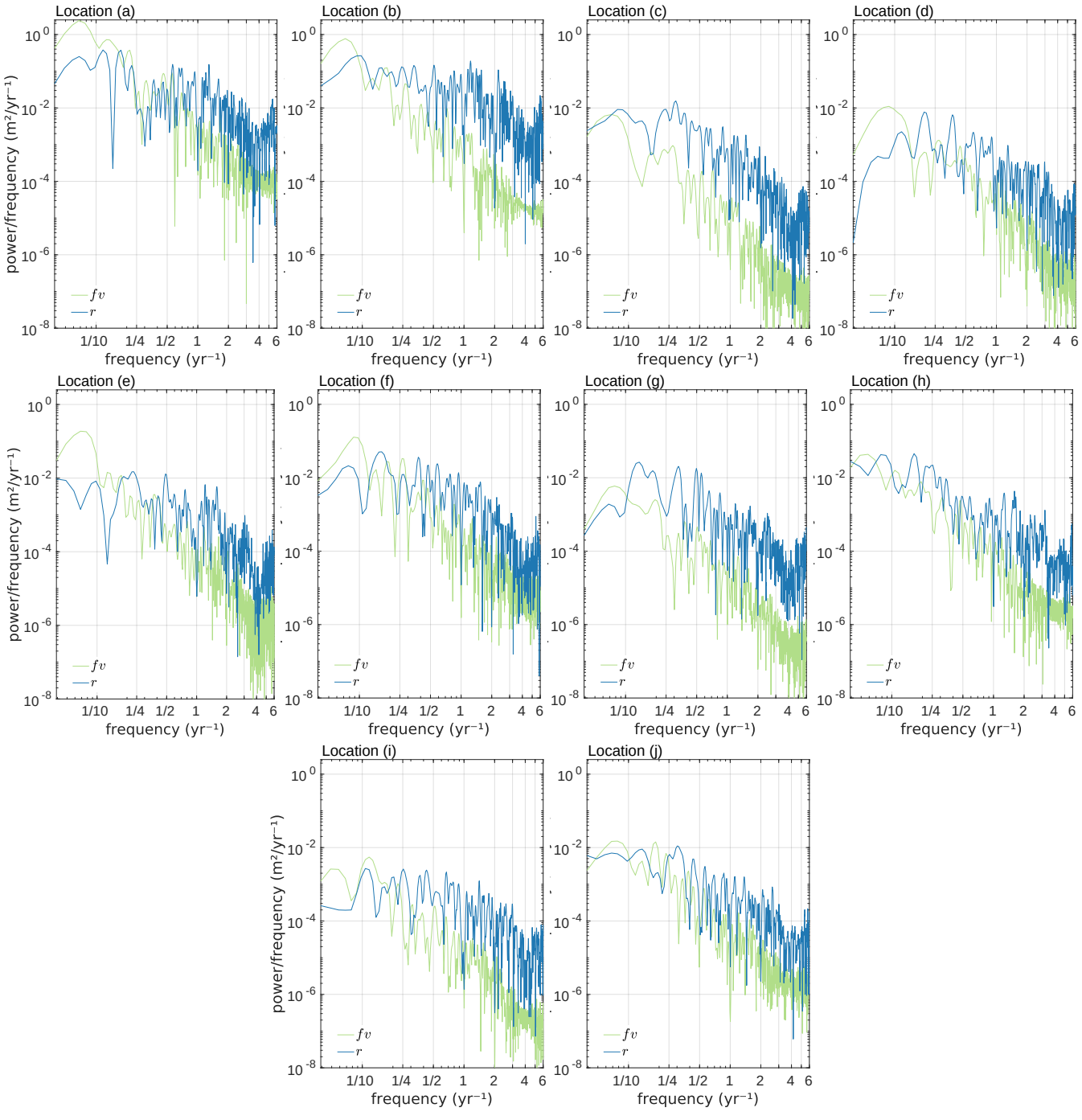

Figure S22. For the subset of selected grid points a–j (Fig. S10), Lomb-Scargle power spectral density (psd) of the altimetric residuals r^{A1a} (blue) and the adjusted firn thickness variations $\mathrm{fv}^{\mathrm{A1a}}$ (green) based on the regression results from version A1a.

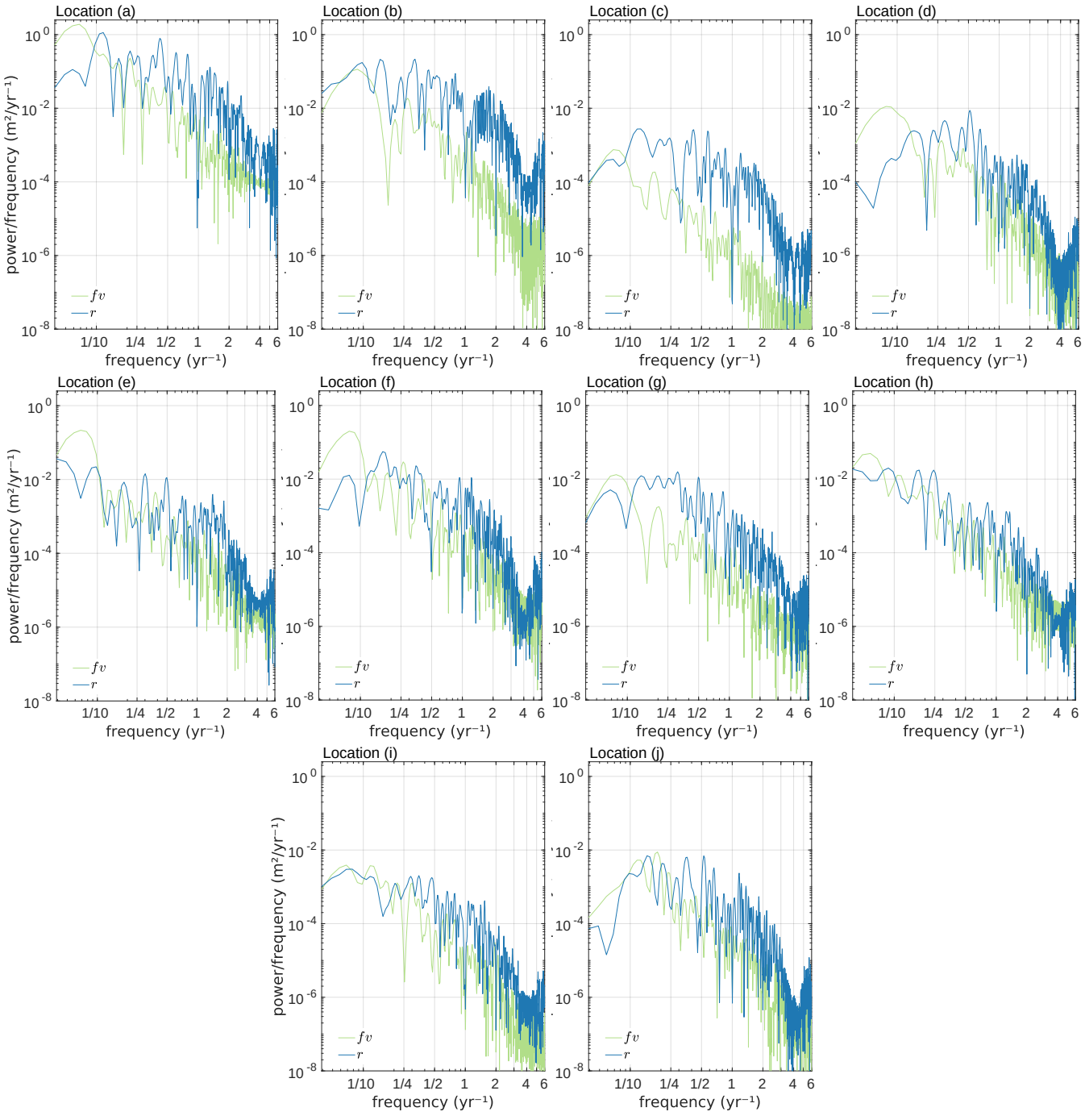

Figure S23. For the subset of selected grid points a–j (Fig. S10), Lomb-Scargle power spectral density (psd) of the altimetric residuals r^{A2a} (blue) and the adjusted firn thickness variations $\mathrm{fv}^{\mathrm{A2a}}$ (green) based on the regression results from version A2a.

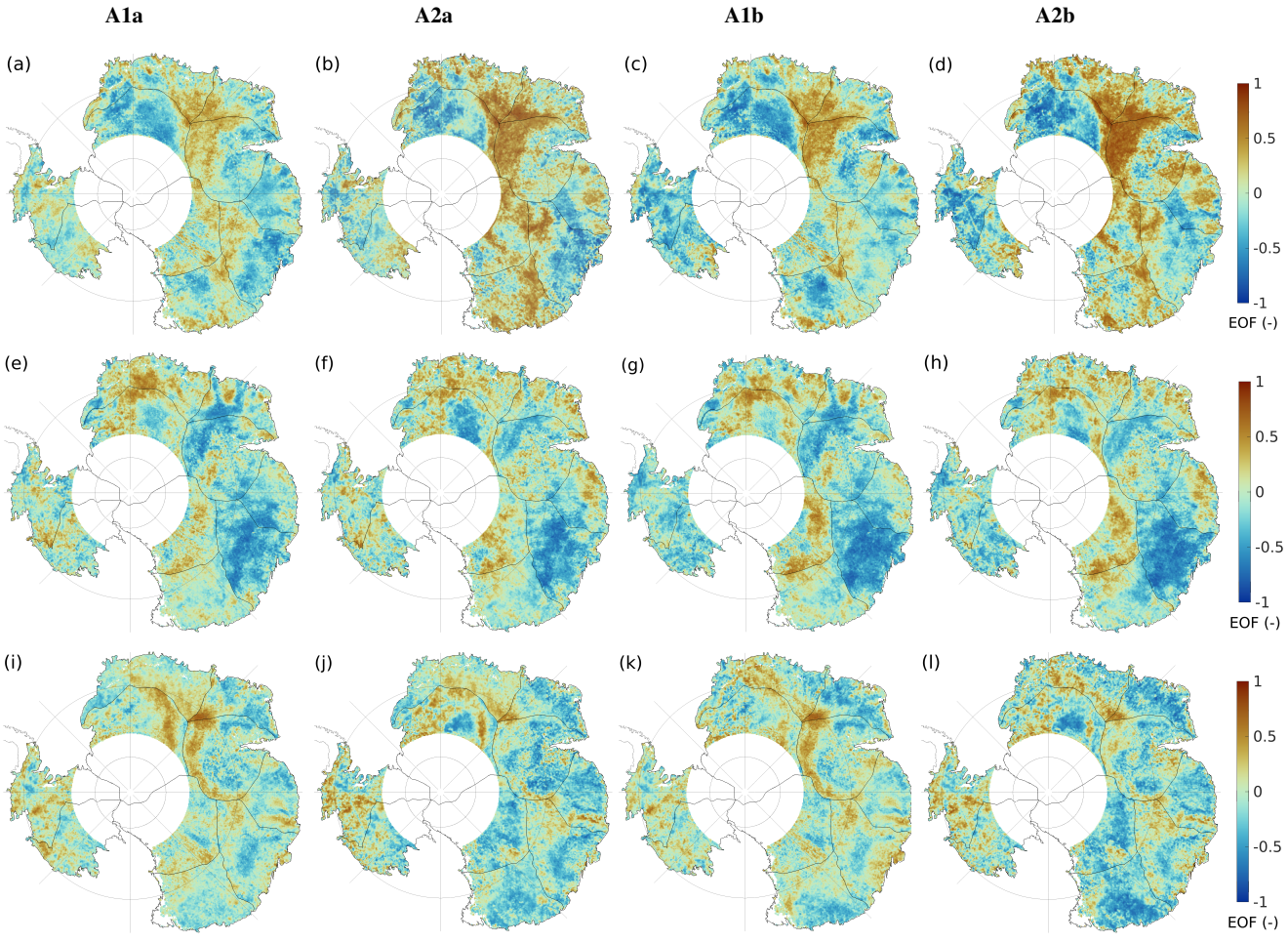

Figure S24. PCA results of standardised altimetric residuals. (a–d) First, (e–h) second and (i–l) third EOFs for r^{A1a} (1st column), r^{A2a} (2nd column), r^{A1b} (3rd column) and r^{A2b} (4th column).

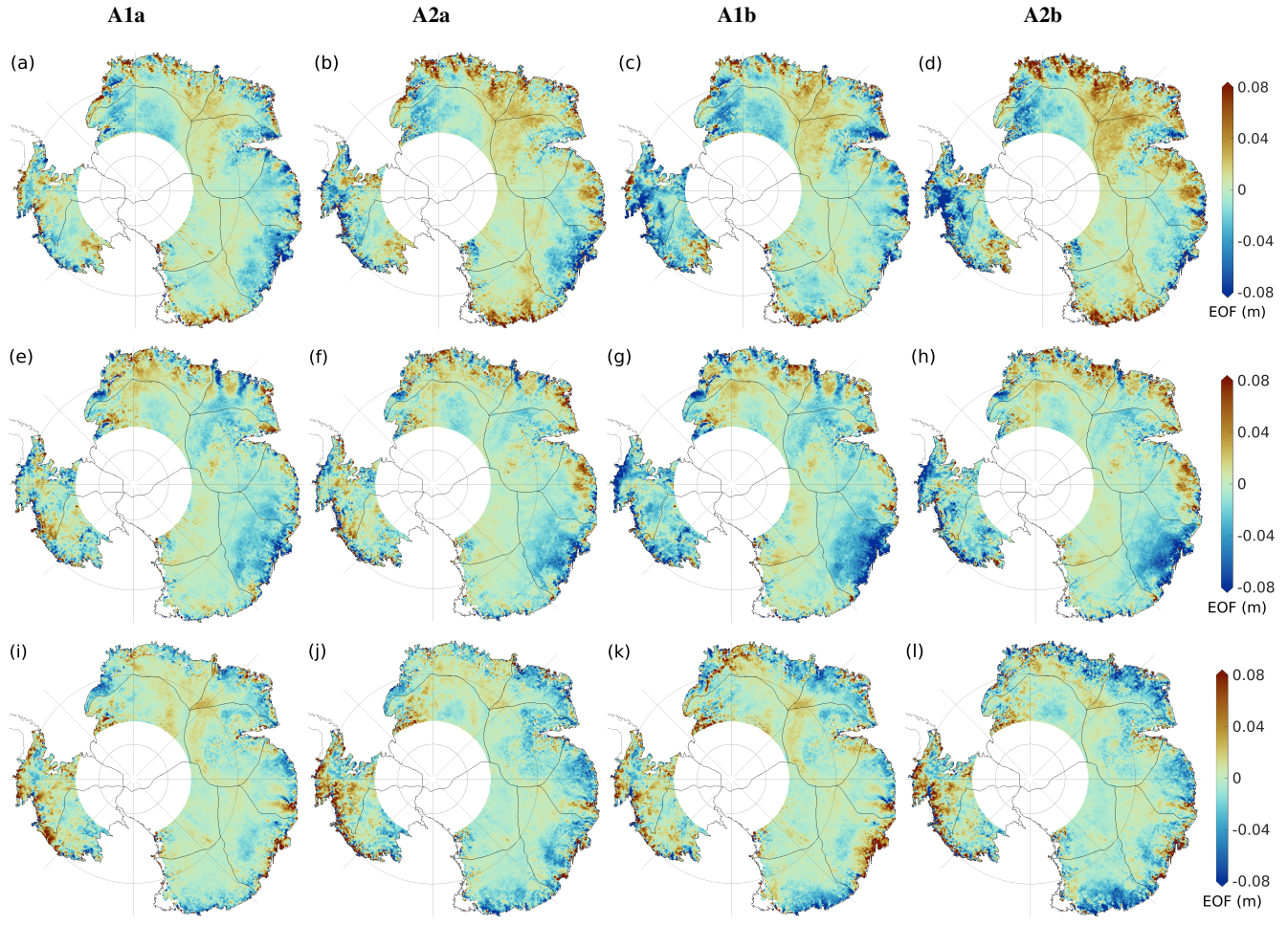

Figure S25. PCA results of standardised altimetric residuals. (a–d) First, (e–h) second and (i–l) third EOFs for r^{A1a} (1st column), r^{A2a} (2nd column), r^{A1b} (3rd column) and r^{A2b} (4th column) with restored signal amplitudes for each grid cell.

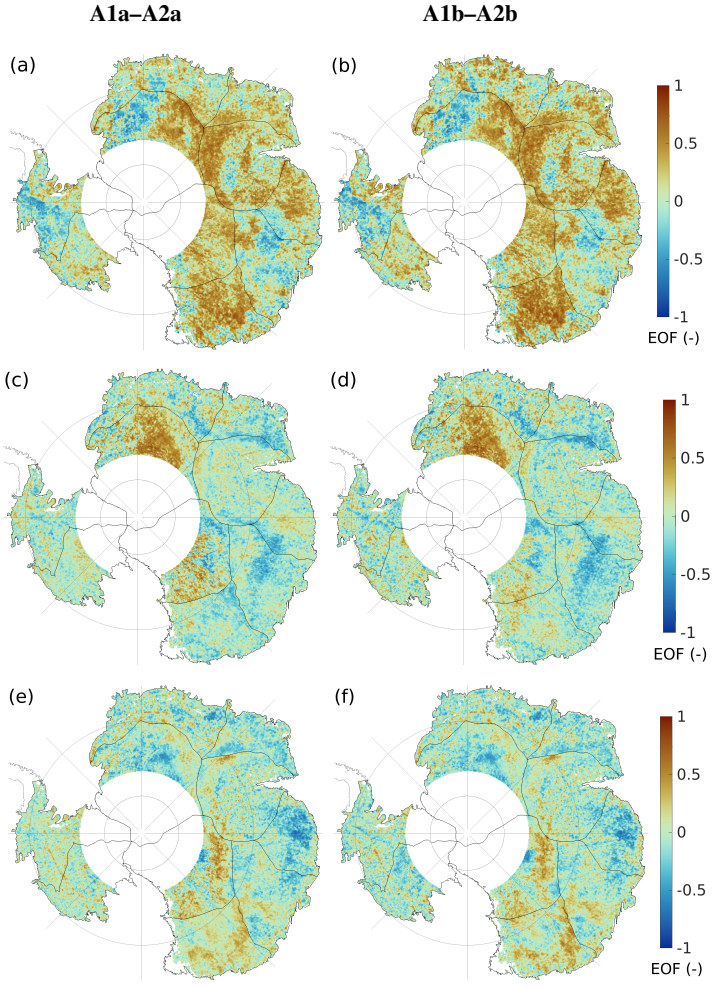

Figure S26. PCA results of standardised altimetric residual differences. (a, b) First, (c, d) second and (e, f) third EOFs for $r^{\mathrm{A1a}} - r^{\mathrm{A2a}}$ (1st column) and $r^{\mathrm{A1b}} - r^{\mathrm{A2b}}$ (2nd column).

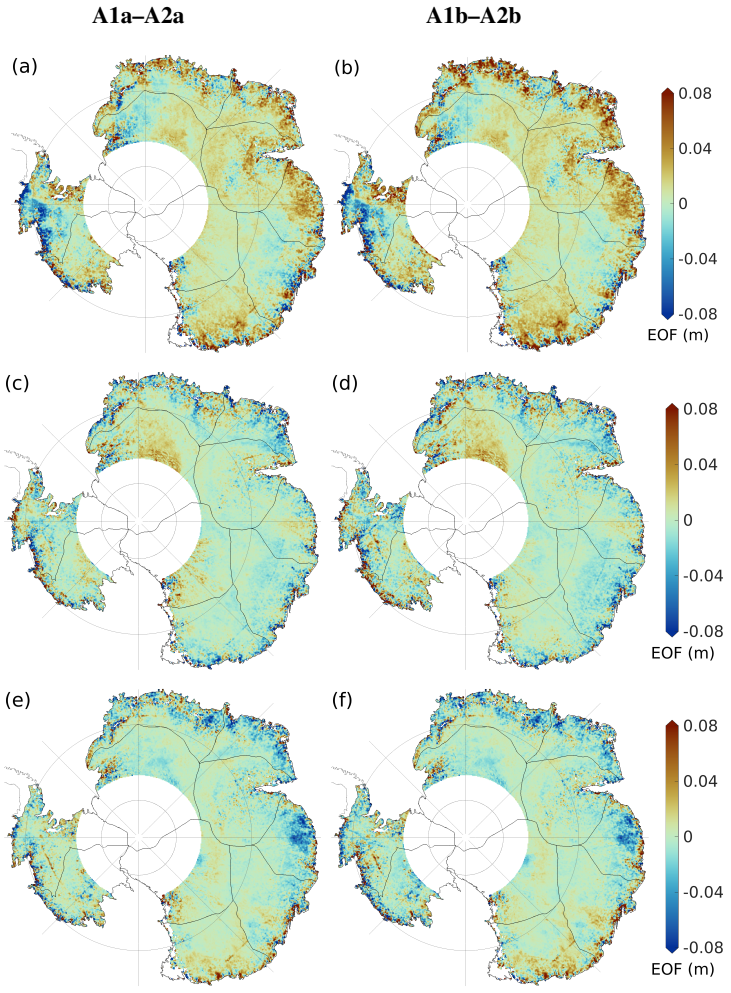

Figure S27. PCA results of standardised altimetric residual differences. (a, b) First, (c, d) second and (e, f) third EOFs for $r^{\mathrm{A1a}} - r^{\mathrm{A2a}}$ (1st column) and $r^{\mathrm{A1b}} - r^{\mathrm{A2b}}$ (2nd column) with restored signal amplitudes for each grid cell.

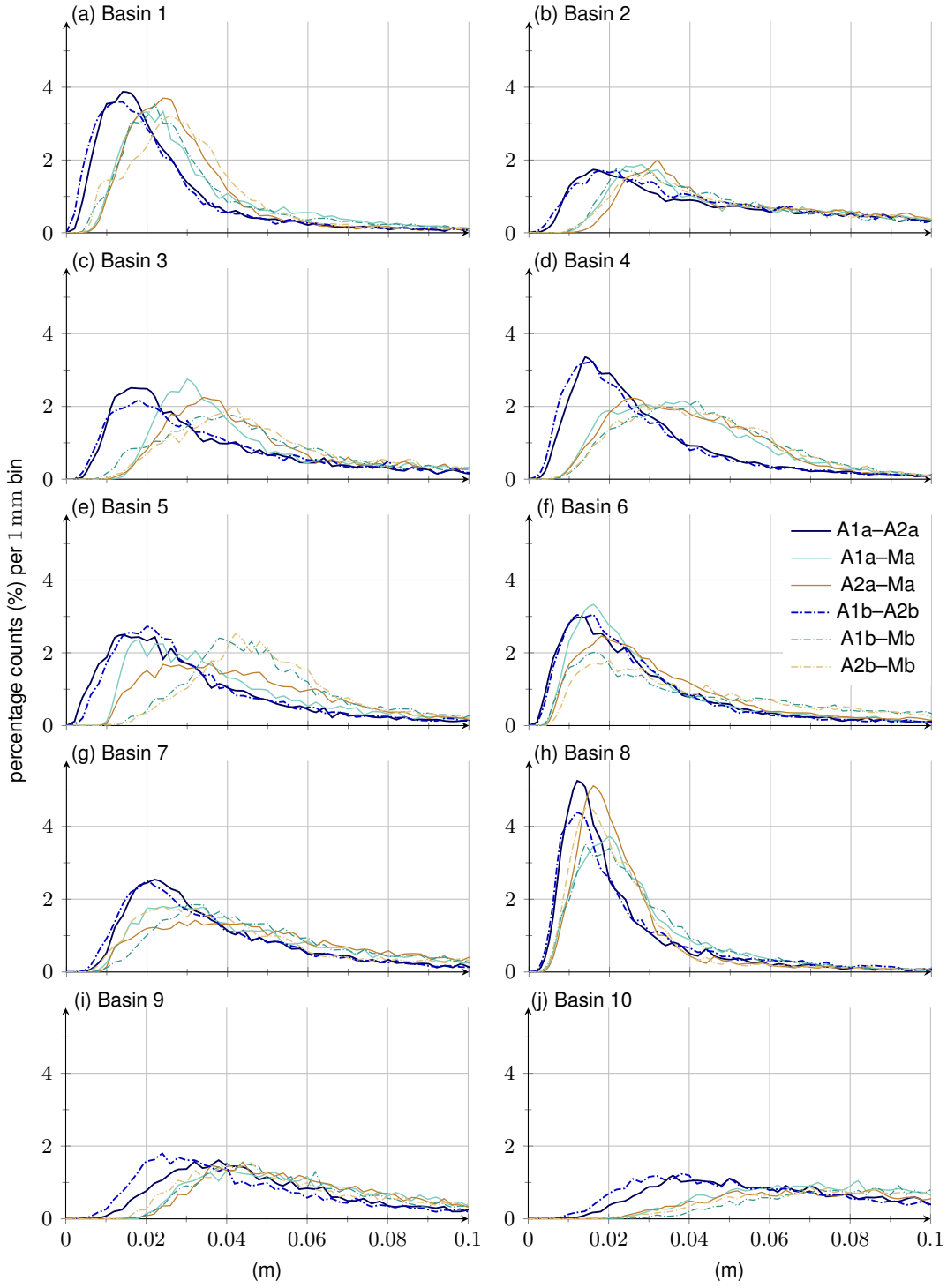

Figure S28. Histograms of the temporal rms of differences between various versions of firn thickness variations based on Ma (solid lines) and Mb (dash-dotted line) for all basins.

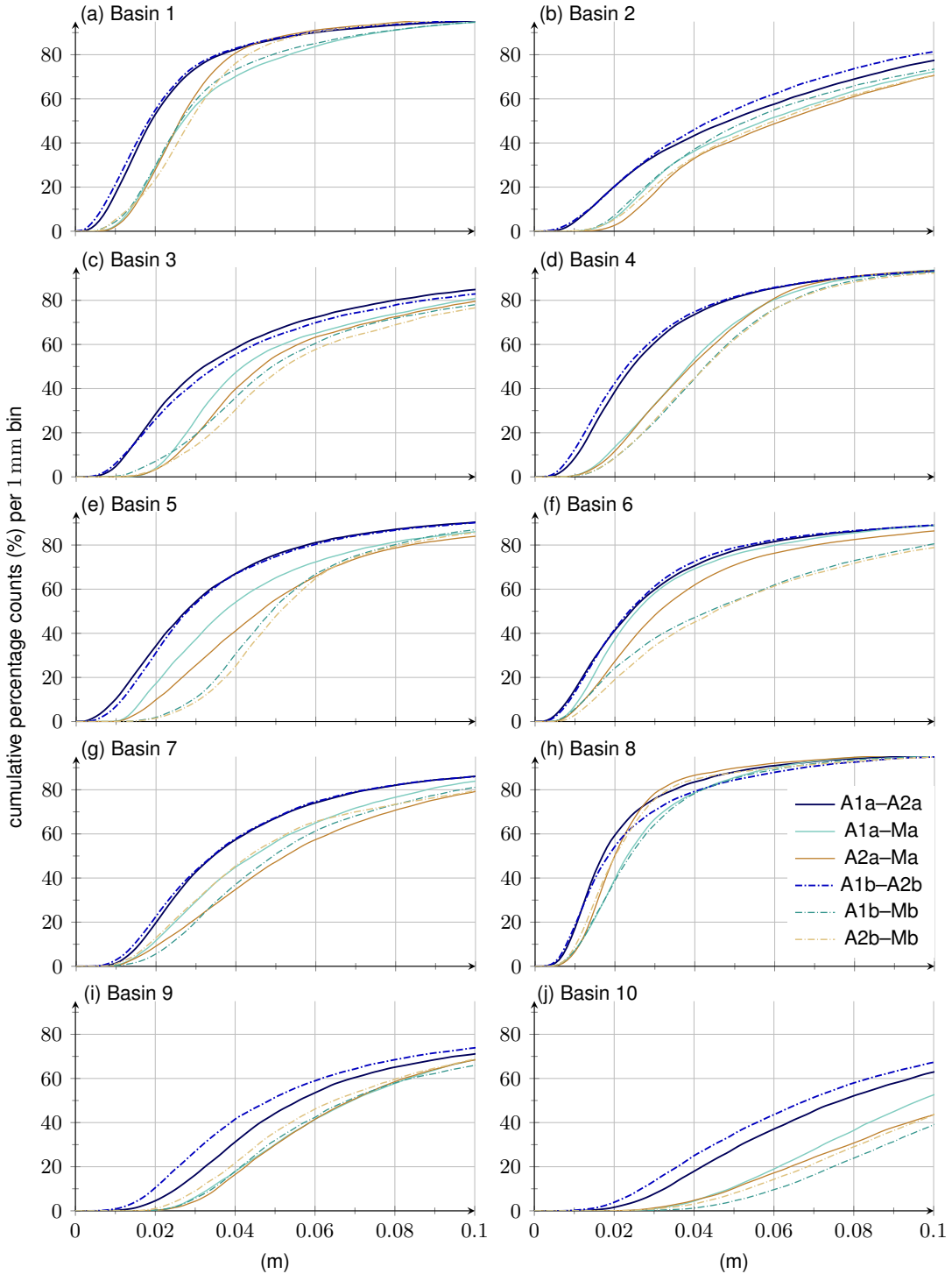

Figure S29. Cumulative histograms of the temporal rms of differences between various versions of firn thickness variations based on Ma (solid lines) and Mb (dash-dotted line) for all basins.

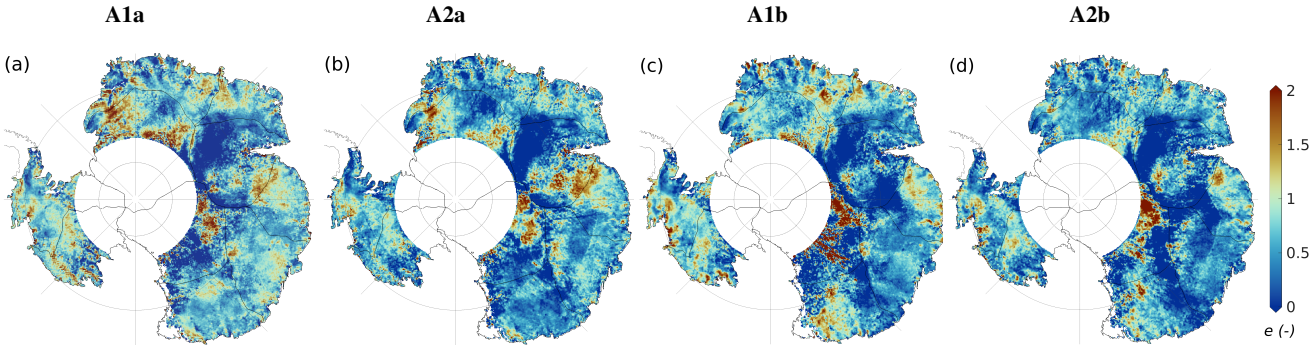

Figure S30. Simple scaling factor e adjusted during the regression approach after experiment E2 (Eq. A2) based on (a) A1a, (b) A2a, (c) A1b and (d) A2b.

References

Medley, B., Neumann, T., Zwally, H., Smith, B., and Stevens, C.: Simulations of firn processes over the Greenland and Antarctic ice sheets: 1980-2021, The Cryosphere, 16, 3971–4011, https://doi.org/10.5194/tc-16-3971-2022, 2022.

Nilsson, J., Gardner, A., and Paolo, F.: Elevation change of the Antarctic Ice Sheet: 1985 to 2020, Earth System Science Data, 14, 3573–3598, https://doi.org/10.5194/essd-14-3573-2022, 2022.

Rignot, E., Mouginot, J., and Scheuchl, B.: Ice Flow of the Antarctic Ice Sheet, Science, 333, 1427–1430, https://doi.org/10.1126/science.1208336, 2011a.

Rignot, E., Mouginot, J., and Scheuchl, B.: Antarctic grounding line mapping from differential satellite radar interferometry, Geophys. Res. Lett., 38, L10 540, https://doi.org/10.1029/2011GL047109, 2011b.

Schröder, L., Horwath, M., Dietrich, R., Helm, V., van den Broeke, M., and Ligtenberg, S.: Four decades of Antarctic surface elevation changes from multi-mission satellite altimetry, The Cryosphere, 13, 427–449, https://doi.org/10.5194/tc-13-427-2019, 2019.

Veldhuijsen, S., van de Berg, W., Brils, M., Kuipers Munneke, P., and van den Broeke, M.: Characteristics of the 1979–2020 Antarctic firn layer simulated with IMAU-FDM v1.2A, The Cryosphere, 17, 1675–1696, https://doi.org/10.5194/tc-17-1675-2023, 2023.